PHYSICAL REVIEW B **93**, 041413(R) (2016)

Chiral plasmon in gapped Dirac systems

Anshuman Kumar,[1] Andrei Nemilentsau,[2] Kin Hung Fung,[3] George Hanson,[2] Nicholas X. Fang,[1,*] and Tony Low[4,†]

[1]*Mechanical Engineering Department, Massachusetts Institute of Technology, Cambridge, Massachusetts 02139, USA*

[2]*Department of Electrical Engineering & Computer Science, University of Wisconsin-Milwaukee, Milwaukee, Wisconsin 53211, USA*

[3]*Department of Applied Physics, The Hong Kong Polytechnic University, Hong Kong, China*

[4]*Department of Electrical & Computer Engineering, University of Minnesota, Minneapolis, Minnesota 55455, USA*

(Received 14 September 2015; revised manuscript received 22 December 2015; published 19 January 2016)

We study the electromagnetic response and surface electromagnetic modes in a generic gapped Dirac material under pumping with circularly polarized light. The valley imbalance due to pumping leads to a net Berry curvature, giving rise to a finite transverse conductivity. We discuss the appearance of nonreciprocal chiral edge modes, their hybridization and waveguiding in a nanoribbon geometry, and giant polarization rotation in nanoribbon arrays.

DOI: 10.1103/PhysRevB.93.041413

Introduction. The Berry curvature is a topological property of the Bloch energy band and acts as an effective magnetic field in momentum space [1–3]. Hence, topological materials may exhibit anomalous Hall-like transverse currents in the presence of an applied electric field, in the absence of a magnetic field. Examples includes topological insulators [4] with propagating surface states that are protected against backscattering from disorder and impurities and transition metal dichalcogenides where the two valleys carry opposite Berry curvature giving rise to bulk topological charge neutral valley currents [5,6]. These bulk topological currents were also experimentally investigated in other Dirac materials, such as a gapped graphene and bilayer graphene system [7,8]. The electromagnetic response of these gapped Dirac systems, particularly that due to its surface electromagnetic modes (i.e., plasmons), are relative unexplored.

In gapped graphene or monolayer transition metal dichalcogenides, electrons in the two valleys have opposite Berry curvature, ensured by time-reversal symmetry (TRS) of their chiral Hamiltonians [5]. Hence, far field light scattering properties of these atomically thin systems does not differentiate between circularly polarized light, i.e., zero circular dichroism in the classical sense. Optical pumping with circularly polarized light naturally breaks TRS, and a net planar chirality ensues. However, under typical experimental conditions, the transverse conductivity due to Berry curvature is less than the quantized conductivity $e^2/\hbar$, and the associated optical dichroism effect is not prominent. These effects, however, can potentially be amplified through enhanced light-matter interaction with plasmons [9–13].

In this Rapid Communication, we discuss the emergence of chiral electromagnetic plasmonic modes and their associated optical dichroism effect. We consider a gapped Dirac system under continuous pumping with circularly polarized light. We discuss the appearance of edge chiral plasmons and how they can allow launching of one-way propagating edge plasmons in a semi-infinite geometry. We also consider the hybridization of these chiral edge modes in a nanoribbon geometry and the possibility of nonreciprocal waveguiding. Their far-field optical properties reveal resonant absorption accompanied by sizable polarization rotation.

Model system. We consider the following Hamiltonian of a massive Dirac system (MDS):

$$\mathcal{H} = \hbar v_f \mathbf{k}\cdot\boldsymbol{\sigma}_\tau + \frac{\Delta}{2}\sigma_z, \tag{1}$$

where $\boldsymbol{\sigma}_\tau = (\tau\sigma_x,\sigma_y)$, $\tau = \pm 1$ denotes the $\mathbf{K}/\mathbf{K}'$ valley, Δ is the energy gap, and v_f is the Fermi velocity. We denote the eigenenergy and wave functions of $\mathcal{H}$ as $\mathcal{E}_{\tau,v}(\mathbf{k})$ and $\Psi_{\tau,v}(\mathbf{k})$, with $v = c,v$ denoting the electron and hole bands. We are interested in the dynamics of the electronic subsystem in an external electromagnetic field $\mathbf{E}$ as illustrated in Fig. 1(a), which can be described with the von Neumann equation, $i\hbar\,\partial_t\hat{\rho} = [\mathcal{H} + V,\hat{\rho}]$, where $\hat{\rho}$ is the statistical operator of the electron subsystem and $V = -e\mathbf{E}\cdot\mathbf{r}$ is the interaction term. In the $\Psi_{\tau,v}(\mathbf{k})$ basis, the equation of motion is written explicitly as [14,15]

$$\begin{aligned}\frac{\partial\rho_{jj'}}{\partial t} + \frac{e}{\hbar}\mathbf{E}\cdot\frac{\partial\rho_{jj'}}{\partial\mathbf{k}} &= -\frac{i}{\hbar}\rho_{jj'}[\mathcal{E}_j(\mathbf{k}) - \mathcal{E}_{j'}(\mathbf{k})] \\ &\quad + \frac{ie}{\hbar}\mathbf{E}\cdot\sum_{j''}[\mathbf{R}_{jj''}(\mathbf{k})\rho_{j''j'} - \rho_{jj''}\mathbf{R}_{j''j'}(\mathbf{k})],\end{aligned} \tag{2}$$

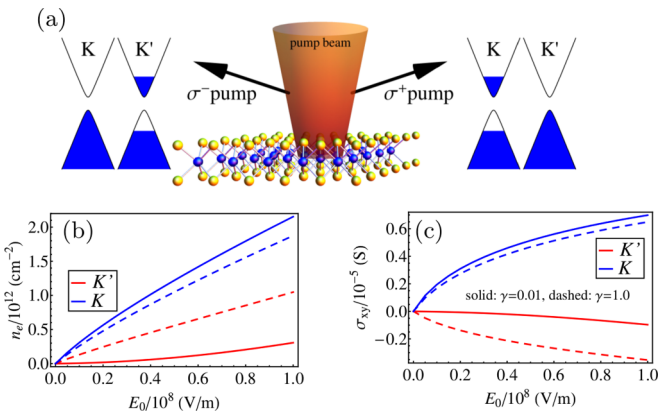

FIG. 1. *Optically induced valley polarization*: (a) Polarization selective pumping leads to different populations in the K and K' valleys. (b) DC electronic carrier concentration in the two valleys as a function of the pump electric field. (c) DC σ_{xy} in the two valleys as a function of the right circular polarized pump electric field.

*nicfang@mit.edu
†tlow@umn.edu

where $[\rho(t,\mathbf{k})]_{j,j'}$ is the density matrix, $\mathbf{R}_{jj'}(\mathbf{k}) = (i/2)\int \Psi^*_j(\mathbf{k})\partial_{\mathbf{k}}\Psi_{j'}(\mathbf{k})d\mathbf{r} + hc$, with $j = \{v,\tau\}$ designating the quantum number of electrons. In Eq. (2) we neglect indirect interband optical transitions.

Here, we are interested in the interaction with a continuous (c.w.) monochromatic electromagnetic wave, $\mathbf{E} = \mathbf{E}_0 e^{-i\omega t} + cc$. Using the rotating wave approximation and introducing relaxation phenomenologically within the relaxation time approximation, we obtain the steady-state solution as a system of four linear equations for diagonal components of the distribution function, $\rho_j \equiv \rho_{jj}$,

$$\rho_{v,\tau}(\mathbf{k}) = \beta_\tau\left(\rho^0_{v,\tau}(\mathbf{k}) + \gamma\rho_{v,\tau'}(\mathbf{k}) + \alpha_\tau\rho_{v',\tau}(\mathbf{k})\right), \qquad (3)$$

where $\tau' \neq \tau$ and $v' \neq v$. Here,

$$\alpha_\tau = \frac{2e^2\left|\mathbf{E}_0\cdot\mathbf{R}^\tau_{cv}(\mathbf{k})\right|^2}{\hbar^2\left[(\omega-\omega_{cv})^2 + 1/\tau_0^2\right]}, \qquad (4)$$

$\omega_{cv} = (\mathcal{E}_{\tau,c} - \mathcal{E}_{\tau,v})/\hbar$, $\beta_\tau = 1/(1+\gamma+\alpha_\tau)$, $\gamma = \tau_0/\tau_1$, where τ_0 is the population relaxation time, and τ_1 is the intervalley scattering time (see Supplemental Material [16]). The equilibrium distribution function is given by the Fermi Dirac distribution, $\rho^0_{v,\tau}(\mathbf{k}) = [1+\exp((\mathcal{E}_{\tau,v}(\mathbf{k})-\mu)/k_BT)]^{-1}$.

Let us consider positive or right circular polarized light, $\mathbf{E}_0 = E_0(\mathbf{e}_x + i\mathbf{e}_y)$, interacting with electrons at the top of the valence band, $\mathbf{R}^\tau_{cv}(\mathbf{0}) = -(v_f\hbar/\Delta)(i\tau\mathbf{e}_x + \mathbf{e}_y)$. It can be clearly seen that $\mathbf{E}_0\cdot\mathbf{R}^\tau_{cv}(\mathbf{0}) = -i(v_f\hbar/\Delta)(\tau+1)$, and thus α_τ, are zero at the $\mathbf{K}'$ valley while being finite at the $\mathbf{K}$ valley. Hence, pumping with circularly polarized light would lead to carrier population imbalance between the two valleys.

Net chirality with pumping. The effective Hamiltonian in Eq. (1) captures the valley physics in a physical system such as monolayer graphene with staggered sublattice potential [17] and transition metal dichalcogenides [5], if the spin-orbit coupling term can be neglected. To proceed, we consider some reasonable numbers for our model gapped Dirac system: an energy gap $\Delta = 0.5$ eV and Fermi velocity $v_f = 1\times 10^6$ ms^{-1}. Our calculations assume temperature $T = 300$ K, typical carrier lifetimes $\tau_0 = 1$ ps, and that the system is undoped at equilibrium. With pumping, charge neutrality and electron-hole symmetry would require that the electron and hole carrier densities follow $n^\tau_e = n^\tau_h$. Fig. 1(b) shows the increasing nonequilibrium electron densities as a function of pump intensities E_0, under continuous wave pumping with right circular polarized light. Finite transfers of electrons from the $\mathbf{K}$ to $\mathbf{K}'$ valley is determined by the intervalley scattering rate described by γ.

In the presence of an external electric field $\mathbf{E}$, the carrier velocity acquires a nonclassical transverse term due to Berry curvature, $\Omega_\tau(\mathbf{k})$, given by $-\frac{e}{\hbar}\mathbf{E}\times\Omega_\tau(\mathbf{k})$. For a MDS, the form of the Berry curvature is well known [5]. Within the semiclassical Boltzmann transport theory, this would give rise to a transverse conductivity, which in the charge neutral case we are considering here is simply given by $\sigma^\tau_{xy} = 2e^2/\hbar\int[d\mathbf{k}]\rho_{c,\tau}(\mathbf{k})\Omega_\tau(\mathbf{k})$. The factor of 2 accounts for contributions from both electrons and holes. It can further be shown that $\sigma^\tau_{xy} = -\sigma^\tau_{yx}$. Since TRS requires $\Omega_{\mathbf{K}}(\mathbf{k}) = -\Omega_{\mathbf{K}'}(\mathbf{k})$, $\sigma^{\mathbf{K}}_{xy} = -\sigma^{\mathbf{K}'}_{xy}$ at equilibrium. However, under continuous wave pumping, the asymmetric carrier populations in the two valleys would produce a net transverse conductivity, as shown in Fig. Fig. 1(c). We note that over the frequency range that we are interested in, i.e., $\hbar\omega \ll \Delta$, σ_{xy} is real and frequency independent [18]. Our calculations suggest that σ_{xy} an order smaller than $e^2/\hbar$ is obtainable with pump intensities E_0 routinely used in pump-probe experiments. The nonequilibrium longitudinal components of the conductivity, $\sigma_{xx} = \sigma_{yy}$, are computed with the Kubo formula [18]. For all subsequent results of this Rapid Communication, we use a pump intensity of $E_0 = 10^8$ V/m and $\gamma = 0.01$.

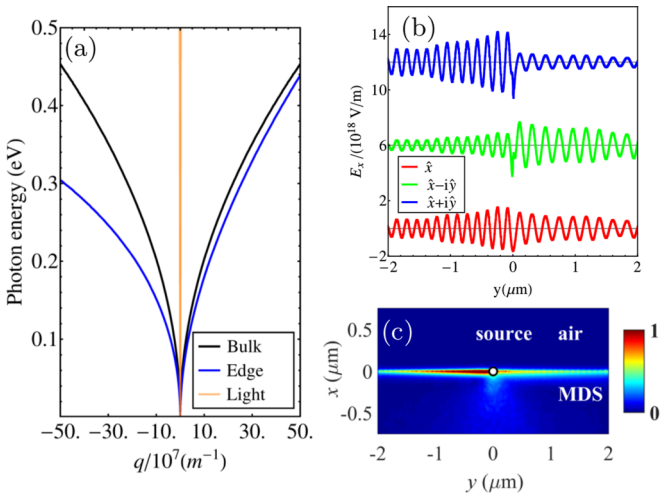

FIG. 2. *(a) Chiral plasmon dispersion in bulk and semi-infinite MDS. (b) Selective excitation of edge modes using circular and linear polarized dipoles placed at the origin:* Line plots of electric field E_x in the plane and perpendicular to the edge. The vertical offset is 6×10^{18} V/m. (c) $|E|$ field (normalized to max) profile for a $\hat{x}$-polarized emitter located near the edge of semi-infinite Dirac material ($x<0$) at $\omega = 0.1$ eV. Both of these field profiles show nonreciprocal emission into the edge mode. The dipoles are placed 10 nm above the MDS.

Valley induced bulk and edge chiral plasmon. Armed with the conductivity sum of the two valleys, σ_{ij}, we discuss general results for the plasmon modes in this system. Plasmon dispersion in a continuous sheet of the MDS is given by [19–21]:

$$\left[\frac{\epsilon_1}{\kappa_1}+\frac{\epsilon_2}{\kappa_2}+\frac{\imath\sigma_{xx}}{\omega\epsilon_0}\right]\cdot\left[\kappa_1+\kappa_2-\frac{\imath\sigma_{yy}}{c\epsilon_0}k_0\right]-\frac{\sigma_{xy}\sigma_{yx}}{(c\epsilon_0)^2}=0, \qquad (5)$$

where $\kappa_{1,2} = \sqrt{q^2-\epsilon_{1,2}k_0^2}$ are the evanescent decay constants on either side of the 2D sheet. As shown in Fig. 2, this "bulk plasmon" dispersion is symmetric with respect to the wave vector q, since it appears quadratically in Eq. (5).

Edges can also accommodate plasmon modes [22]. Symmetry arguments show that although bulk plasmon dispersion respects $\omega(\mathbf{q}) = \omega(-\mathbf{q})$ with the nonsymmetric conductivity tensor, the presence of an edge can break this degeneracy [23]. Here we consider the case of semi-infinite MDS. Within the quasistatic picture, the edge plasmon dispersion is approximately given by [22,24]: $\eta^2 - \chi^2 - 3\eta + 2\sqrt{2}\chi\ \mathrm{sgn}(q) = 0$, where $\eta = |q|\sigma_{xx}/(\imath\epsilon_0\epsilon\omega)$ and $\chi = |q|\sigma_{xy}/(\epsilon_0\epsilon\omega)$. Fig. 2(a) indeed shows that the right moving edge plasmon has a different dispersion compared to the left moving one. A simple

realization of this nonreciprocity effect consists of placing a dipole near the edge of the material. Finite element simulation of near field dipole emission was performed using COMSOL. As shown in Figs. 2(b) and 2(c), the linear dipole preferentially emits into the left propagating edge state. Taking a cue from Ref. [25], we can also use a circular dipole to couple emission into the left or right edge state, depending on dipole helicity. The results for circular dipoles are presented in Fig. 2(b).

In terms of experiment, the appropriate plasmon momentum can be selected either by use of a grating near the edge [26] or by adjusting the distance between the tip of a near field microscope and the edge of the MDS or the tip radius [27–29]. Since the edge plasmon dispersion is nonreciprocal, selection of the magnitude of the plasmon momentum will also lead to selectivity in the propagation direction. In addition to the different intensities of the two, the different wavelengths for the left and right moving edge modes in this configuration might be used for nonreciprocal phase shifters [30].

Waveguiding in nanoribbons. Any practical realization of the semi-infinite case discussed above will involve a stripe or waveguide geometry. Waveguides are an important component of plasmonic circuitry [31], and ribbon waveguides based on the plasmon modes in graphene have been proposed [32,33]. In this section, we show how the chirality of the plasmon leads to the propagation direction being coupled to the ribbon edge. It should be noted that unlike the semi-infinite case for ribbons placed in homogeneous space, the dispersion of these plasmon modes is symmetric due to the presence of spatial symmetry [23]. However, these modes show nonreciprocity with respect to edge localization as discussed below.

As shown in Fig. 3, qualitatively the typical profile of plasmons in ribbon [32,33] or nanowire [34] geometries is observed: There is an acoustic branch arising from a monopolelike mode and a discrete set of higher order guided modes which show a cutoff. The high frequency field profiles of the two lowest order modes (for example, $1'$ and $2'$ for $k_z > 0$) in Fig. 3 reveal that these modes have the character of edge modes in semi-infinite MDS. In fact, these edge modes of the ribbon lie outside the "cone" of the bulk plasmon mode for the continuous MDS. As we approach lower frequencies, the edge localization of these two modes becomes weaker and they start hybridizing.

All the other modes are guided modes with field maxima in the bulk. These lie inside the cone formed by the dispersion of the plasmon in continuous MDS. Thus these modes are analogous to the guided modes in slab waveguides. The cutoff frequencies for all except the lowest mode are consistent with the Fabry-Perót condition, $k_B w + \phi_R = n\pi$, where k_B is the bulk plasmon momentum in the MDS, as given by Eq. (5), and $\phi_R \approx -3\pi/4$ is the approximate phase acquired by the plasmon upon reflection from the ribbon edge [35].

The chirality of the plasmon mode in our case gives rise to the coupling between the propagation direction and the edge. For instance, for positive k_z, at higher frequencies, we observe that the field is only confined to the left edge for the lowest mode. Such a coupling is useful for enhancing the lifetime of the mode propagating in a given direction.

This special coupling between the edge mode direction and the ribbon edge can be utilized to produce explicit nonreciprocal devices. For instance, we can break the spatial symmetry between left and right by introducing another medium on one side of the ribbon. In the most extreme case, a perfect conductor can be used to short the edge mode on one side [30].

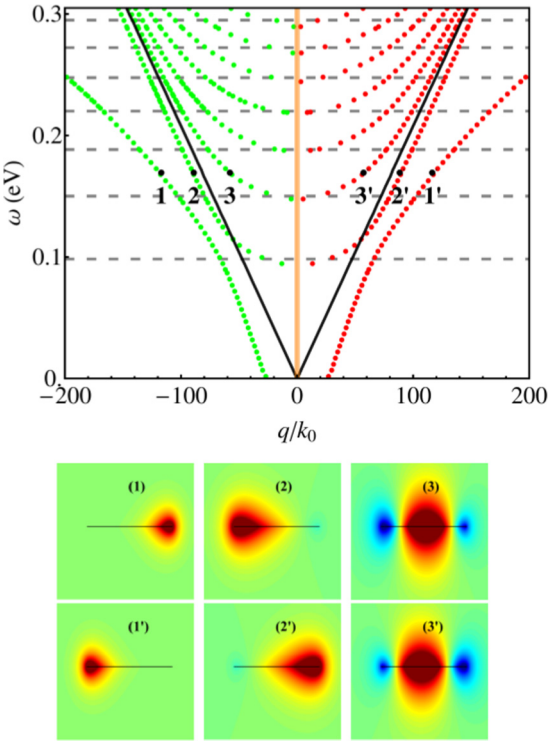

FIG. 3. *Guided modes in freestanding MDS ribbons.* Ribbon width is assumed to be $w = 100$ nm. The gray dashed lines represent solutions of $k_B w + \phi_R = n\pi$, where k_B is the bulk plasmon momentum in MDS and $\phi_R \approx -3\pi/4$ [35], which explains the cutoff for all the guided modes (except the edge mode). The black solid lines represent the bulk plasmon in a continuous sheet of MDS (same as Fig. 2). The color plots below represent the real part of the electric field along the ribbon at the indicated q.

Valley induced giant polarization rotation. Polarization rotation is usually discussed in the context of magneto-optical materials (also called Faraday effect), where the plane of polarization of the incident wave is rotated upon passage through such a material [36]. Cyclotron resonances in various two-dimensional electron gases [37] were employed to produce this effect, with graphene being the most promising candidate [38]. Optically induced valley polarization in a MDS presents a promising route to achieve a similar effect without the application of a static magnetic field, which can be cumbersome in the context of on-chip photonic components miniaturization.

We first consider polarization rotation in a continuous sheet of MDS. The polarization rotation angle is given by [39] $\theta_F \approx \Re\{\sigma_{xy}\}/2c\epsilon_0$ and the transmission by $T(\omega) \approx 1 - \Re\{\sigma_{xx}\}/c\epsilon_0$. It should be noted that as opposed to optical activity [40] which is reciprocal, the polarization rotation in our case is analogous to Faraday rotation which is a purely nonreciprocal effect [41]. These equations suggest that the polarization rotation values in the continuous 2D sheet are only dependent on the σ_{xy}, which

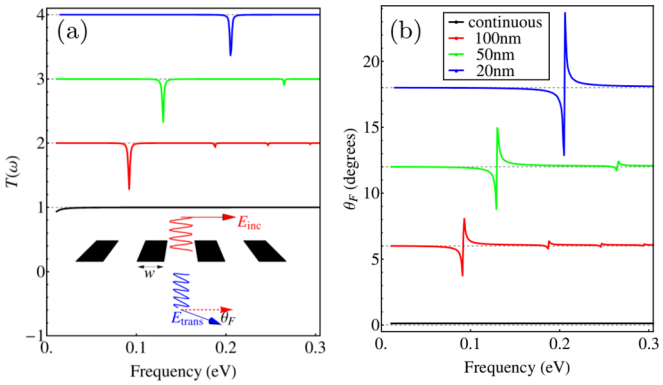

FIG. 4. *Transmission and polarization rotation in freestanding MDS ribbons*: (a) Transmission (vertical offset is one unit). Inset: Schematic of the configuration. Note that in general the transmitted wave is expected to be elliptically polarized as opposed to linear as shown here. (b) Polarization rotation spectrum for different ribbon sizes w (vertical offset is 6 degrees). For ribbon arrays, a filling factor of 50% has been assumed.

can be tuned by adjusting the intensity and polarization of the pump. Even with a pump intensity of the order of 10^8 V/m, rotation angle of only about 0.1 degrees is obtained.

However, it is possible to use localized plasmon resonances [42,43] of nanoribbons [44] to enhance the polarization rotation values. In Fig. 4, we present the simulation results for transmission and polarization rotation in nanoribbons. We obtain significant enhancement of polarization rotation by more than an order of magnitude upon using nanoribbons as opposed to a continuous 2D sheet. Moreover, at the frequency of the resonant enhancement, transmitted intensity is still about 10–20%. The spectral location of the resonance is strongly tunable as a function of the ribbon width. These frequencies correspond to the solutions of $k_B w + \phi_R = n\pi$, as described earlier but with the constraint that n is an even integer [35]. Odd n solutions are nondipolar modes, hence do not couple with normally incident plane waves. The largest polarization rotation occurs for smaller ribbon sizes. This is because smaller ribbons correspond to larger in-plane wave vectors, thus providing a higher field confinement. The polarization rotation we obtained with nanoribbons was found to even surpass Faraday rotation angles in monolayer graphene under a magnetic field of 7 T [38].

Conclusion and summary. In summary, we have shown how polarization selective pumping in a generic gapped Dirac material can impart chirality to bulk and edge plasmons without the need for an external magnetic field. Experimentally testable predictions in the context of near field imaging, giant valley induced polarization rotation, as well as nonreciprocal waveguiding were presented. Our theoretical approach can be applied to a general class of two dimensional gapped Dirac materials. A rich array of nonreciprocal phenomenon can be potentially explored, from the point of view of applications to isolators, circulators, etc. Finally, since unlike the case of applied magnetic field, the field profile of the optical pump can be easily manipulated on the subwavelength scale by the use of nanostructures [45], our work might pave the way for chip scale nonreciprocal photonics and optically tunable metasurfaces [46,47].

Note added in proof. Recently, we became aware of a related preprint [48].

Acknowledgments. A.K. and N.X.F. acknowledge the financial support by the NSF (Grant No. CMMI-1120724) and AFOSR MURI (Award No. FA9550-12-1-0488). K.H.F. acknowledges financial support from Hong Kong RGC Grant No. 15300315. T.L. acknowledges support from the MRSEC Program of the National Science Foundation under Award No. DMR-1420013.

[1] M. V. Berry, in *Proceedings of the Royal Society of London A: Mathematical, Physical and Engineering Sciences*, Vol. 392 (The Royal Society, London, 1984), pp. 45–57.
[2] D. Xiao, M.-C. Chang, and Q. Niu, Rev. Mod. Phys. **82**, 1959 (2010).
[3] N. Nagaosa, J. Sinova, S. Onoda, A. MacDonald, and N. Ong, Rev. Mod. Phys. **82**, 1539 (2010).
[4] M. Z. Hasan and C. L. Kane, Rev. Mod. Phys. **82**, 3045 (2010).
[5] D. Xiao, G.-B. Liu, W. Feng, X. Xu, and W. Yao, Phys. Rev. Lett. **108**, 196802 (2012).
[6] K. F. Mak, K. L. McGill, J. Park, and P. L. McEuen, Science **344**, 1489 (2014).
[7] R. Gorbachev, J. Song, G. Yu, A. Kretinin, F. Withers, Y. Cao, A. Mishchenko, I. Grigorieva, K. Novoselov, L. Levitov *et al.*, Science **346**, 448 (2014).
[8] M. Sui, G. Chen, L. Ma, W. Shan, D. Tian, K. Watanabe, T. Taniguchi, X. Jin, W. Yao, D. Xiao *et al.*, arXiv:1501.04685.
[9] A. N. Grigorenko, M. Polini, and K. S. Novoselov, Nat. Photonics **6**, 749 (2012).
[10] F. H. L. Koppens, D. E. Chang, and F. J. Garcia de Abajo, Nano Lett. **11**, 3370 (2011).
[11] M. Jablan, H. Buljan, and M. Soljačić, Phys. Rev. B **80**, 245435 (2009).
[12] T. Low and P. Avouris, ACS Nano **8**, 1086 (2014).
[13] G. Giuliani and G. Vignale, *Quantum Theory of the Electron Liquid* (Cambridge University Press, Cambridge, 2005).
[14] G. Y. Slepyan, A. A. Khrutchinski, A. M. Nemilentsau, S. A. Maksimenko, and J. Herrmann, Int. J. Nanosci. **03**, 343 (2004).
[15] A. Nemilentsau, G. Slepyan, A. Khrutchinskii, and S. Maksimenko, Carbon **44**, 2246 (2006).
[16] See Supplemental Material at http://link.aps.org/supplemental/10.1103/PhysRevB.93.041413 for details of the calculation of the evolution of the system under external electromagnetic field, incorporation of relaxation times and steady state populations.
[17] A. C. Neto, F. Guinea, N. Peres, K. S. Novoselov, and A. K. Geim, Rev. Mod. Phys. **81**, 109 (2009).
[18] Z. Li and J. P. Carbotte, Phys. Rev. B **86**, 205425 (2012).
[19] K. W. Chiu and J. J. Quinn, Phys. Rev. B **9**, 4724 (1974).
[20] G. Hanson, IEEE Trans. Antennas Propag. **56**, 747 (2008).
[21] D. Yudin, O. Eriksson, and M. I. Katsnelson, Phys. Rev. B **91**, 075419 (2015).

[22] A. L. Fetter, Phys. Rev. B **32**, 7676 (1985).
[23] R. Camley, Surf. Sci. Rep. **7**, 103 (1987).
[24] W. Wang, J. M. Kinaret, and S. P. Apell, Phys. Rev. B **85**, 235444 (2012).
[25] B. le Feber, N. Rotenberg, and L. Kuipers, Nat. Commun. **6**, 6695 (2015).
[26] H. Raether, *Surface Plasmons on Smooth and Rough Surfaces and on Gratings* (Springer, Berlin, 1988) .
[27] Z. Fei, G. O. Andreev, W. Bao, L. M. Zhang, A. S. McLeod, C. Wang, M. K. Stewart, Z. Zhao, G. Dominguez, M. Thiemens, M. M. Fogler, M. J. Tauber, A. H. Castro Neto, C. N. Lau, F. Keilmann, and D. N. Basov, Nano Lett. **11**, 4701 (2011).
[28] Z. Fei, A. S. Rodin, G. O. Andreev, W. Bao, A. S. McLeod, M. Wagner, L. M. Zhang, Z. Zhao, M. Thiemens, G. Dominguez, M. M. Fogler, A. H. Castro Neto, C. N. Lau, F. Keilmann, and D. N. Basov, Nature (London) **487**, 82 (2012).
[29] J. Chen, M. Badioli, P. Alonso-Gonzlez, S. Thongrattanasiri, F. Huth, J. Osmond, M. Spasenović, A. Centeno, A. Pesquera, P. Godignon, A. Z. Elorza, N. Camara, F. J. G. de Abajo, R. Hillenbrand, and F. H. L. Koppens, Nature (London) **487**, 77 (2012).
[30] D. L. Sounas and C. Caloz, Appl. Phys. Lett. **99**, 231902 (2011).
[31] Y. Fang and M. Sun, Light Sci. Appl. **4**, e294 (2015).
[32] A. Y. Nikitin, F. Guinea, F. J. García-Vidal, and L. Martín-Moreno, Phys. Rev. B **84**, 161407 (2011).
[33] J. Christensen, A. Manjavacas, S. Thongrattanasiri, F. H. L. Koppens, and F. J. García de Abajo, ACS Nano **6**, 431 (2012).
[34] A. Manjavacas and F. J. García de Abajo, Nano Lett. **9**, 1285 (2009).
[35] A. Y. Nikitin, T. Low, and L. Martin-Moreno, Phys. Rev. B **90**, 041407 (2014).
[36] M. Faraday, Philos. Trans. R. Soc. Lond. **136**, 1 (1846).
[37] M. Suzuki, K. ichi Fujii, T. Ohyama, H. Kobori, and N. Kotera, J. Phys. Soc. Jpn. **72**, 3276 (2003).
[38] I. Crassee, J. Levallois, A. L. Walter, M. Ostler, A. Bostwick, E. Rotenberg, T. Seyller, D. van der Marel, and A. B. Kuzmenko, Nat. Phys. **7**, 48 (2011).
[39] A. Ferreira, J. Viana-Gomes, Y. V. Bludov, V. Pereira, N. M. R. Peres, and A. H. Castro Neto, Phys. Rev. B **84**, 235410 (2011).
[40] S. Zhang, J. Zhou, Y.-S. Park, J. Rho, R. Singh, S. Nam, A. K. Azad, H.-T. Chen, X. Yin, A. J. Taylor, and X. Zhang, Nat. Commun. **3**, 942 (2012).
[41] R. J. Potton, Rep. Prog. Phys. **67**, 717 (2004).
[42] B. Sepúlveda, J. B. González-Díaz, A. García-Martín, L. M. Lechuga, and G. Armelles, Phys. Rev. Lett. **104**, 147401 (2010).
[43] Y. Hadad, A. R. Davoyan, N. Engheta, and B. Z. Steinberg, ACS Photonics **1**, 1068 (2014).
[44] M. Tymchenko, A. Y. Nikitin, and L. Martn-Moreno, ACS Nano **7**, 9780 (2013).
[45] S. A. Maier, *Plasmonics: Fundamentals and Applications* (Springer, New York, 2007).
[46] A. Fallahi and J. Perruisseau-Carrier, Appl. Phys. Lett. **101**, 231605 (2012).
[47] A. V. Kildishev, A. Boltasseva, and V. M. Shalaev, Science **339** 1232009 (2013).
[48] J. C. W. Song and M. S. Rudner, arXiv:1506.04743.